Atmos. Chem. Phys. Discuss., 12, 19571–19615, 2012
www.atmos-chem-phys-discuss.net/12/19571/2012/
doi:10.5194/acpd-12-19571-2012


Atmospheric Chemistry and Physics Discussions



# Upwelling into the lower stratosphere forced by breaking tropical waves: evidence from chemical tracers

**Z. Engida and I. Folkins**

Department of Physics and Atmospheric Science, Dalhousie University Halifax, B3H 3J5, Nova Scotia, Canada

Received: 4 July 2012 – Accepted: 21 July 2012 – Published: 7 August 2012

Correspondence to: Z. Engida (zelalem.engida@dal.ca)

Published by Copernicus Publications on behalf of the European Geosciences Union.

## Abstract

Measurements from the Microwave Limb Sounder (MLS) on the 68 hPa pressure level from 1 January 2005 to 31 December 2010 are used to calculate the coherence between anomalies in the tropical mean mixing ratios of $H_2O$, CO, and $N_2O$, and 100 hPa temperature. We show that the fluctuations of lower stratospheric water vapor in the subseasonal and multiyear time windows are generated by different physical mechanisms. In the subseasonal time window, the spatial pattern of the coherence between 100 hPa temperature and water vapor, and the time lag, show that the variability in lower stratospheric water vapor is dominated by fluctuations in upwelling forced by the dissipation of tropical Rossby waves. In the multiyear time window, the variability of lower stratospheric water vapor is more strongly coherent with temperature fluctuations on the 100 hPa surface in regions where the annual mean temperature is colder than 194 K. In addition, the 68 hPa water vapor anomalies lag the 100 hPa temperature anomalies by roughly 140 days. In this time window, the variability of lower stratospheric water vapor is therefore dominated by changes in the temperature dependent dehydration efficiency which modulate the water vapor stratospheric entry mixing ratio. On subseasonal timescales, the spatial pattern of the coherence between 100 hPa temperature and 68 hPa CO anomalies is very similar to the pattern of coherence between 100 hPa temperature and the Real-time Multivariate MJO series 1 (RMM1) index of the Madden Julian Oscillation (MJO). The MJO therefore has a strong influence on the subseasonal variability of CO in the lower stratosphere. The subseasonal 68 hPa CO and $H_2O$ anomalies lag the 100 hPa temperature anomalies by 3.16 and 2.51 days, respectively. The similarity between the two time lags suggests that the subseasonal CO anomalies can also be attributed to changes in upwelling. The multiyear variability in lower stratospheric $N_2O$ appears to be dominated by the Quasi Biennial Oscillation (QBO).





ACPD
12, 19571–19615, 2012

## 1 Introduction

The chemical composition of the stratosphere is strongly affected by the composition of the air upwelling across the tropopause into the stratosphere. Until recently, it was believed that this upward flow was driven by the breaking and momentum transfer of waves in the extratropics (Holton et al., 1995). However, there is increasing evidence, from both diagnostic interpretations of reanalysis data (Kerr-Munslow and Norton, 2006; Randel et al., 2008) and model simulations (Boehm and Lee, 2003; Norton, 2006; Garny et al., 2011b) that much of the upwelling in the lower tropical stratosphere is forced by the dissipation of tropical waves. This upwelling source has been called the Boehm-Lee-Norton (BLN) mechanism (Ryu and Lee, 2010). We provide additional support for this mechanism by demonstrating that much of the tracer variability in tropical lower stratosphere is coherent with tropical Rossby wave activity.

On multiyear timescales, tracer variability in the lower stratosphere is dominated by upwelling variability associated with the El Nino Southern Oscillation (ENSO) (Garcia and Randel, 2008; Randel et al., 2009; Calvo et al., 2010) and the Quasi Biennial Oscillation (QBO) (Randel et al., 2004; Fueglistaler and Haynes, 2005; Schoeberl et al., 2008). It is therefore most appropriate to look for tracer variability from the BLN mechanism on subseasonal timescales (30–90 days). The main source of variance in convective activity in this time window is the Madden Julian Oscillation (MJO). During MJO events, a large envelope of enhanced convection propagates eastward across the Indian Ocean toward the Western Pacific at a speed of 5–8 $\mathrm{m\,s^{-1}}$ (Zhang, 2005; Monier et al., 2010). MJO events modulate the generation of Rossby waves, and should therefore generate fluctuations in the mixing ratios of chemical tracers in the lower stratosphere through the BLN mechanism.

Rossby waves generate wind and pressure anomalies which have characteristic horizontal patterns near the tropical tropopause (Ryu and Lee, 2010). We compare these patterns with maps of the coherence between temperature anomalies on the 100 hPa surface and anomalies in tropical mean lower stratospheric tracer mixing ratios. We



Discussion Paper | Discussion Paper | Discussion Paper | Discussion Paper |

ACPD

12, 19571–19615, 2012

Upwelling into the lower stratosphere

Z. Engida and I. Folkins

interpret similarities between the two maps, in the subseasonal time window, as evidence that tracer variability in the lower stratosphere is forced by Rossby waves. We also calculate maps of the coherence between 100 hPa temperature fluctuations and tropical mean lower stratospheric tracer anomalies in the multiyear time window. These maps are compared with the pattern of temperature fluctuations on the 100 hPa surface associated with ENSO and the QBO.

**Paper overview**

The datasets used in the paper are described in Sect. 2. We use measurements of water vapor ($H_2O$), carbon monoxide (CO), and nitrous oxide ($N_2O$) from the Microwave Limb Sounder (MLS) (Waters et al., 2006). The $H_2O$ measurements from MLS were compared with measurements from the Atmospheric Chemistry Experiment-Fourier Transform Spectrometer (ACE-FTS) instrument (Bernath et al., 2005). This comparison is discussed in the Appendix. In defining the 100 hPa temperature anomalies, we considered the use of three different reanalysis datasets. This section explains our choice of temperature data from the Modern Era Retrospective Analysis for Research and Application (MERRA) reanalysis. We also discuss how the temperature and chemical tracer anomalies are defined, and in particular, the procedures for the removal of the mean value, trend, seasonal cycle, and short timescale variability from each time series.

In Sect. 3, we outline the calculation of the coherence between the anomalies in tropical (15° S–15° N) mean 100 hPa temperature and the anomalies in the tropical (20° S–20° N) mean 68 hPa mixing ratios of the chemical tracers. Peaks in the tropical mean coherence spectrum are interpreted as spectral regions where lower stratospheric tracer anomalies are more strongly coupled to 100 hPa temperature anomalies, and used to select the subseasonal and multiyear time windows.

The main diagnostic used in this paper is a recently introduced quantity referred to as the $\bar{\kappa}$ statistic (Oliver and Thompson, 2010). As used here, $\bar{\kappa}^2$ refers to the variance



ACPD
12, 19571–19615, 2012

in the tropical mean mixing ratio of a chemical tracer that can be attributed to the temperature anomalies of a particular grid cell on the 100 hPa surface, normalized by the observed variance of the chemical tracer. The relationship between temperature fluctuations on the 100 hPa surface and the fluctuations in the mixing ratio of a chemical tracer will vary with frequency, depending on the relative importance of the relevant dynamical modes. In Sect. 4, we calculate maps of the $\bar{\kappa}$ statistic in the subseasonal and multiyear time windows. For the subseasonal time window, we compare the $\bar{\kappa}$ maps of the chemical tracers with $\bar{\kappa}$ maps generated using the Real-time Multivariate MJO series 1 (RMM1) index (Wheeler and Hendon, 2004). For the multiyear time window, the $\bar{\kappa}$ maps of the various chemical tracers are compared with $\bar{\kappa}$ maps generated from the QBO and ENSO indices.

Convective heating along the equator generates a characteristic boomerang pattern in dynamical anomalies, with Rossby lobes extending westward from the heat source on both sides of the equator (Gill, 1980; Hendon and Salby, 1994; Jin and Hoskins, 1995; Ting and Yu, 1998; Tian et al., 2006; Ryu and Lee, 2010). This Rossby wave pattern, and its induced lower stratospheric upwelling, evolve over a roughly 16 days period subsequent to the onset of convective heating at the equator (Ryu and Lee, 2010). In the lower stratosphere, fluctuations in upwelling associated with the BLN mechanism will occur at a variety of frequencies, depending on the variance in the generation of Rossby waves by tropical convection. For tracers with vertical gradients, changes in upwelling introduce modifications in the local tendency for vertical advection. The tracer anomalies themselves can therefore be expected to be out of pahse with the upwelling anomalies. If changes in lower stratospheric upwelling can be regarded as roughly in phase with 100 hPa temperature anomalies, tracer anomalies from the BLN mechanism should lag 100 hPa temperature anomalies. If the phase offset between lower stratospheric tracer anomalies and 100 hPa temperature anomalies is independent of frequency, the time interval between the 100 hPa temperature anomalies and the response of a lower tropospheric tracer should increase with the period of the upwelling anomaly.





ACPD
12, 19571–19615, 2012

In the case of water vapor, there is a second mechanism through which changes in upwelling can be expected to generate anomalies in the lower stratosphere. An upwelling increase at the tropical tropopause will increase the rate of adiabatic expansion cooling. In this case, air parcels being advected horizontally and vertically through the TTL will be exposed to colder temperatures, and a greater frequency of dehydration events. Due to the slow ascent rates of the lower stratosphere (Randel et al., 2008), the time lag associated with the appearance of negative water vapor anomalies in the lower stratosphere will be considerably longer than time lag discussed above in association with wave induced changes in vertical advection. This difference in time lags, between the onset of temperature fluctuations on the 100 hPa surface and the occurrence of a water vapor anomaly in the lower stratosphere, provides a method for helping attribute the origin of water vapor anomalies in the lower stratosphere to a particular physical mechanism. In Sect. 5, we therefore calculate the time lags in both the subseasonal and multiyear time windows. In Sect. 6, we summarize the main results of the paper and discuss its relationship with previous work.

## 2 Description of datasets

### 2.1 MLS: $H_2O$, CO and $N_2O$

The Microwave Limb Sounder (MLS) (Waters et al., 2006) is one of four instruments on the National Aeronautics and Space Administration (NASA) Earth Observing Satellite (EOS) Aura satellite, launched on 15 July 2004. Although Aura/MLS started taking observations on 13 August 2004, this paper focuses on 1 January 2005–31 December 2010 time period. Aura is in a sun-synchronous near-circular polar orbit as a member of the constellation of satellites called the A train. MLS observes microwave emission from molecules such as $H_2O$, CO, $N_2O$ in five spectral regions from 118 GHz to 2.5 THz using seven radiometer devices. The altitude range of MLS is from near the ground to ~90 km and near global in the horizontal, (82° S–82° N). The MLS can





ACPD
12, 19571–19615, 2012

take measurements during the day and night, and in the presence of ice clouds and aerosols that would normally prevent measurements by most other sensors.

This paper uses MLS level 2, v3.3 $H_2O$, CO and $N_2O$ measurements (Waters et al., 2006; Lambert et al., 2007; Read et al., 2007; Vömel et al., 2007). $H_2O$ is reported on 55 pressure levels, while CO and $N_2O$ are reported on 37 pressure levels. The vertical resolution for $H_2O$ ranges between 2.0 to 3.7 km for pressure levels 316–0.22 hPa, while the along track horizontal resolution is ∼ 210–360 km for pressures greater than 4.61 hPa. The across track resolution is 7 km for all pressures. In the TTL, the vertical and along track resolution of the CO measurements is 3.5–5 km and ∼ 700 km, respectively. The vertical and along track resolutions of the $N_2O$ measurements are 4–6 km and 300–600 km, respectively. Erroneous profiles have been screened using status and quality flags, convergence, and precision fields (Lambert et al., 2007; Read et al., 2007). Profiles with odd status and negative precision outside prescribed quality and convergence fields were rejected. Cloud status fields are more important below the 100 hPa pressure level and were not used (Lambert et al., 2007). Negative values were considered valid, since their rejection would give rise to positive bias in the tropical daily mean averages.

### 2.2 ACE: $H_2O$

The ACE-FTS instrument uses solar occultation (up to 15 sunrises and 15 sunsets occultations per day) geometry to obtain vertical profiles of up to 82 species (Bernath et al., 2005). It was launched on the Scientific Satellite-1 (SCISAT-1), and has been taking measurements since January 2004. We use version 3.0 water vapor measurements from this instrument to compare with the 68 hPa MLS water vapor measurements. Due to the satellite orbit, ACE-FTS measurements from the tropics are available for about four months per year.





ACPD

12, 19571–19615, 2012

## 2.3 Temperature

### 2.3.1 ERA-Interim

ERA-Interim is a global atmospheric reanalysis produced by the European Centre for Medium-Range Weather Forecasts, (ECMWF), and is available from 1979 to the present (Dee and Uppala, 2009). Atmospheric model and data assimilation techniques are improved from ERA-40 (Bouttier and Rabier, 1997). ERA-Interim has 37 pressure levels and a horizontal resolution of $1.5^\circ \times 1.5^\circ$. We used the four times per day temperature analyses, obtained from the ECMWF website (http://data-portal.ecmwf.int/data/d/interim_daily/levtype=pl/), to calculate daily mean values at 100 hPa for 2005–2010. ERA-Interim is a global analysis and has a coarse vertical spacing near the tropopause. We chose 100 hPa as the level nearest the tropopause in the 30° N–30° S latitude range.

### 2.3.2 NCEP

The National Center for Environmental Prediction (NCEP) (Kalnay et al., 1996) provides a global reanalysis product during the period 1948–present. The NCEP reanalysis has a horizontal resolution of $2.5^\circ \times 2.5^\circ$, and 17 pressure levels. The NCEP 100 hPa reanalysis temperature data were obtained from the NOAA/PSD website (http://www.esrl.noaa.gov/psd/).

### 2.3.3 MERRA

The Modern Era Retrospective Analysis for Research and Application, (MERRA), uses NASA's GEOS-5 data assimilation system (GEOS-5 DAS) (Rienecker et al., 2008). The data archive covers the period from 1979–present. The GEOS-5 model has a native resolution of $2/3^\circ$ longitude by $1/2^\circ$ degree latitude (Bosilovich et al., 2008; Rienecker et al., 2011) but the daily temperatures are reported on a $1.25^\circ \times 1.25^\circ$ grid. The model has 72 vertical levels extending from surface to 0.01 hPa. The 100 hPa temperatures





ACPD
12, 19571–19615, 2012

used in this work are obtained from the NASA Goddard Earth Sciences Data and Information Services Center (GES DISC) website (http://mirador.gsfc.nasa.gov/).

### 2.4 MJO and QBO/ENSO indices

We use the first of the two multivariate MJO indices (RMM1) obtained from the Centre for Australian Weather and Climate Research website (http://cawcr.gov.au/staff/mwheeler/maproom/RMM/RMM1RMM2.74toRealtime.txt). RMM1 is the first Principal Component (PC) time series that form the index called the Real-time Multivariate MJO series 1 (RMM1), (Wheeler and Hendon, 2004).

Monthly QBO indices come from Climate Prediction Center (CPC) website at National Oceanic and Atmospheric Administration (NOAA) (http://www.cpc.ncep.noaa.gov/data/indices/). The zonally averaged wind index (formally called Singapore winds) anomalies at 30 and 50 hPa are used as proxies for QBO. In this paper we use only the 50 hPa component.

Monthly data for Global Sea Surface Temperature (SST) ENSO indices (defined as the average SST anomaly equatorward of 20° latitude (north and south) minus the average SST poleward of 20°) are obtained from the university of Washington website, (http://jisao.washington.edu/data/globalsstenso/).

### 2.5 Data preparation

#### 2.5.1 Selection of MLS pressure level

Figure 1 shows the averaging kernels of v3.3 MLS $H_2O$ measurements on the 82 hPa ($\sim$ 17.7 km) and 68 hPa ($\sim$ 18.8 km) pressure levels, obtained from the MLS webpage (http://mls.jpl.nasa.gov/data/ak/). The 82 hPa kernel extends significantly below the 100 hPa level into the troposphere. Although the 68 hPa averaging kernel also has some weighting below 100 hPa, this weighting should be sufficiently small that the MLS measurements on this pressure level are most reflective of the stratospheric entry





ACPD
12, 19571–19615, 2012

mixing ratio. Although the MLS averaging kernels are species dependent to some extent, we also use CO and $N_2O$ measurements on the 68 hPa level.

The 100–50 hPa pressure range of the 68 hPa averaging kernel shown in Fig. 1 corresponds to a height range of roughly 4 km (16.6–20.6 km). The annual mean upwelling velocity between 17 and 20 km is roughly 0.25 mm s$^{-1}$ ($\sim$8 km yr$^{-1}$) (Randel et al., 2008). An air parcel would therefore require about 200 days to vertically traverse the full depth of the MLS averaging kernel. The 68 hPa MLS measurements are therefore unlikely to capture changes in the stratospheric entry tracer mixing ratio of a chemical tracer on time scales less than a month.

### 2.5.2 Selection of MERRA reanalysis for 100 hPa temperature

The dotted, dashed, and solid lines in Fig. 2a refer to ERA-Interim, NCEP and MERRA 100 hPa temperatures respectively, averaged between 15° N and 15° S, from 2005 to 2010. Temperatures from the NCEP reanalysis were roughly 2 K higher than the other two from early-2005 to mid-2007 (Randel et al., 2000; Wong and Dessler, 2007). After mid-2007, NCEP temperatures are usually colder than ERA-Interim and MERRA. ERA-Interim and MERRA temperatures are usually in good agreement between 2005 and 2010. Figure 2b shows 15-day Lanczos low pass filtered (Duchon, 1979) deseasonalized anomalies of the temperature time series shown in Fig. 2a. This figure shows more clearly the 2005 to mid-2007 warm bias, and 2008–2010 cold bias, of the NCEP reanalyses relative to ERA-Interim and MERRA.

Figure 2c–e shows scatterplots of the reanalysis temperature anomalies against one another. The MERRA and ERA-Interim temperature anomalies are in best agreement, with a correlation $r = 0.906$, and slope $b = 0.785$. The two plots involving NCEP temperature anomalies indicate a tendency for the points to segregate into two groups. This splitting reflects the warm and cold biases of NCEP temperature anomalies in the periods before and after mid-2007 discussed earlier. Given the greater consistency of the MERRA and ERA-Interim reanalyses, and the finer spatial resolution of the MERRA





ACPD
12, 19571–19615, 2012

reanalysis, we use MERRA temperatures in our subsequent analysis. However, the results are similar to those obtained using ERA-Interim temperatures.

#### 2.5.3 Anomaly calculations

Figure 3a–c shows the variation in tropical mean (20° S–20° N) MLS $H_2O$, CO, and $N_2O$ from 2005 to 2010 on the 68 hPa surface. Figure 3d shows the variation of (15° S–15° N) mean MERRA temperature on the 100 hPa surface. Figure 4a–d shows the anomalies in tropical mean $H_2O$, CO, and $N_2O$, and temperature, respectively. The anomalies were calculated from the tropical mean values by removal of the 6 yr (2005–2010) mean, removal of the seasonal cycle by subtraction of the annual and semi-annual harmonics, and removal of the linear trends. Our results do not strongly depend on whether the trend is removed or retained. There is also a 15-day low pass Lanczos filtering applied to all daily data to minimize noise.

In Fig. 4e the solid and dashed lines refer to anomalies in monthly mean 100 hPa (re-scaled) temperature (15° N–15° S) and 68 hPa water vapor (20° N–20° S), respectively. From 2005 to early 2009, the water vapor anomalies lag temperature anomalies by several months. The solid and dashed lines of Fig. 4f refer to monthly mean zonal wind anomalies at 50 hPa (U50) and the ENSO (re-scaled) index respectively. The U50 line shows a periodicity of approximately 2 yr. Each of the monthly time series has been smoothed (for plotting purpose only) by applying a 3-month low pass filter.

#### 2.5.4 Exclusion of the first 600 days from $N_2O$ time series

Nitrous oxide and carbon monoxide have common surface sources and are positively correlated in the tropical troposphere (D'Amelio et al., 2009). In Fig. 5, the $N_2O$ anomaly is plotted against the CO anomaly for the 2005–2010 period. Measurements within the first 600 days are indicated with open circles, while measurements from day 601 to day 2191 are indicated with gray plus signs. $N_2O$ and CO are anticorrelated during the first 600 days with a negative slope $b = -0.315$ and a correlation $r = -0.232$. During the remaining time period, $N_2O$ and CO are positively correlated with a positive slope $b = 0.426$ and $r = 0.337$. The origin of the change in sign of the correlation is unclear. It may arise from difficulties associated with the definition of the anomalies of the two tracers, and in particular, the parameterization of the seasonal cycle in terms of the two harmonics, or the assumption that the two species have linear trends. However, because the second part of the $N_2O$ anomaly time series was more consistent with other measurements than the first part, the first 600 days were removed from the $N_2O$ time series.

## 3 Method

### Coherence squared, $\kappa^2$

To calculate the coherence squared ($\kappa^2$) between anomalies in 68 hPa tropical mean MLS $H_2O$ and tropical mean 100 hPa 15° N–15° S MERRA temperature, we first define the auto-covariance functions of temperature, $\gamma_T$, water vapour, $\gamma_{H_2O}$, and the cross-covariance function, $\gamma_{T,H_2O}$, (e.g. Hans and Francis, 2003).

$$\gamma_T(\tau) = \frac{1}{N-1}\sum_{t=1}^{N}(T(t))(T(t+\tau)) \tag{1a}$$

$$\gamma_{H_2O}(\tau) = \frac{1}{N-1}\sum_{t=1}^{N}(H_2O(t))(H_2O(t+\tau)) \tag{1b}$$

$$\gamma_{T,H_2O}(\tau) = \frac{1}{N-1}\sum_{t=1}^{N}(T(t+\tau))(H_2O(t+\tau)) \tag{1c}$$

$N$ refers to the total number of days, $T(t)$ and $H_2O(t)$ to the temperature and water vapor anomaly daily time series from Fig. 4b, and $\tau$ to a specified time lag. When



ACPD
12, 19571–19615, 2012

$\tau = 0$, the auto-covariance functions $\gamma_T$ and $\gamma_{H_2O}$ reduce to the variances $\sigma_T^2$ and $\sigma_{H_2O}^2$, while the cross-covariance function, $\gamma_{T,H_2O}$, is reduced to the covariance $\sigma_{T,H_2O}^2$.

For all frequencies $\omega \in [-\frac{1}{2}, \frac{1}{2}]$ (in units of cycles per day), the $\gamma$'s are then Fourier transformed to give the individual power spectra $\Gamma_T(\omega)$, $\Gamma_{H_2O}(\omega)$, and the cross-spectrum, $\Gamma_{T,H_2O}(\omega)$ (Priestley, 1981).

$$\Gamma_T(\omega) = \sum_{\tau=-\infty}^{\infty} \gamma_T(\tau)\, e^{-2\pi\, i\tau\omega} \tag{2a}$$

$$\Gamma_{H_2O}(\omega) = \sum_{\tau=-\infty}^{\infty} \gamma_{H_2O}(\tau)\, e^{-2\pi\, i\tau\omega} \tag{2b}$$

$$\Gamma_{T,H_2O}(\omega) = \sum_{\tau=-\infty}^{\infty} \gamma_{T,H_2O}(\tau)\, e^{-2\pi\, i\tau\omega} \tag{2c}$$

Figure 6 shows the power spectra of the temperature and tracer anomalies. Each power spectrum has been normalized by the number of daily values ($N$) and the appropriate variance. Due to the removal of the annual and semi annual cycles, the spectra exhibit minima near periods of 0.5 yr and 1 yr. The temperature and $H_2O$ power spectra have strong QBO features. The $N_2O$ spectrum has a weaker QBO feature. All tracer spectra exhibit variability within the MJO window (30–90 days), but the power is usually weaker than at longer periods.

The cross-spectrum, $\Gamma_{T,H_2O}(\omega)$, can be expressed in a polar coordinate form as

$$\Gamma_{T,H_2O}(\omega) = A_{T,H_2O}(\omega)\, e^{i\Phi_{T,H_2O}(\omega)} \tag{3}$$

where $A_{T,H_2O}$ and $\Phi_{T,H_2O}$ are the amplitude and phase spectra respectively. The amplitude spectrum can then be used to define the coherence squared between temperature





ACPD
12, 19571–19615, 2012

and water vapor.

$$\kappa^2_{\mathrm{T,H_2O}}(\omega) = \frac{A^2_{\mathrm{T,H_2O}}(\omega)}{\Gamma_{\mathrm{T}}(\omega)\Gamma_{\mathrm{H_2O}}(\omega)} \tag{4}$$

The squared coherence $\kappa^2_{\mathrm{T,H_2O}}(\omega)$ reduces the complex valued cross-spectrum function, $\Gamma(\omega)_{\mathrm{T,H_2O}}$ to a real-valued function of frequency. $\kappa^2_{\mathrm{T,H_2O}}(\omega)$ is constrained to have a value between 0 and 1, with 0 indicating an absence of coherence, and 1 indicating the maximum possible coherence.

Figure 7a shows the coherence squared $\kappa^2_{\mathrm{T,H_2O}}$ between tropical mean 68 hPa $H_2O$ and 100 hPa MERRA temperature. There is a strong narrow peak within the MJO band (Zhang, 2005) centered at 82 days, and a broad maximum at periods longer than 2 yr. The width of this maximum suggests that multiyear variability in tropical mean 100 hPa temperature anomalies gives rise to a similar response in water vapor, whether the temperature forcing comes from the QBO or has some other dynamical origin (e.g. ENSO).

Figure 7b shows the coherence squared of tropical mean 68 hPa CO and $N_2O$ with 100 hPa MERRA temperature. CO has a significant coherence with temperature in the MJO window, where there are three distinct peaks. $N_2O$ also exhibits peaks within the MJO window, in addition to coherence on multiyear timescales.





ACPD
12, 19571–19615, 2012



Z. Engida and I. Folkins

## 4 The $\bar{\kappa}$ statistic

### 4.1 Derivation

The observed variance of water vapor ($\sigma^2_{H_2O}$) over a given frequency window $[\omega_1, \omega_2]$ can be calculated from the power spectrum $\Gamma_{H_2O}$.

$$\sigma^2_{H_2O} = \int_{\omega_1}^{\omega_2} \Gamma_{H_2O}(\omega)d\omega \tag{5}$$

The portion of the variance in water vapor that can be attributed to (or "predicted" by) temperature is given by (Priestley, 1981),

$$\sigma^2_p = \int_{\omega_1}^{\omega_2} \kappa^2_{T,H_2O}(\omega)\Gamma_{H_2O}(\omega)d\omega \tag{6}$$

The $\bar{\kappa}$ statistic is defined as the square root of the predicted variance normalized by the observed variance (Oliver and Thompson, 2010).

$$\bar{\kappa}_{T,H_2O} = \sqrt{\frac{\sigma^2_p}{\sigma^2_{H_2O}}} \tag{7}$$

### 4.2 Spatial patterns in $\bar{\kappa}$

We use the definition of $\bar{\kappa}$ given in Eq. (7) to calculate the fraction of the variance in the tropical mean 68 hPa mixing ratio of a chemical tracer that can be attributed to MERRA temperature fluctuations at individual grid cells on the 100 hPa surface. The spatial pattern of a $\bar{\kappa}$ map will depend on the time window over which it is defined. We calculate $\bar{\kappa}$ using particular frequency windows in Eqs. (5) and (6). These frequency windows were chosen by inspection from Fig. 7, where they are indicated by red boxes.





ACPD
12, 19571–19615, 2012



Title Page
Abstract | Introduction
Conclusions | References
Tables | Figures
◀| |▶
◀ ▶
Back | Close
Full Screen / Esc
Printer-friendly Version
Interactive Discussion

### 4.3 Subseasonal time window

The upper panel of Fig. 7 shows that the coherence between tropical mean 68 hPa water vapor and 100 hPa MERRA temperature is enhanced in the 74–107 days time window. Fig. 8a shows the $H_2O$ $\bar{\kappa}$ map generated using this subseasonal time window. The most prominent features of this map are two arcs of high $\bar{\kappa}$ on both sides of the equator straddling the western Indian Ocean and Africa, and appearing to originate from a location near the equator west of Indonesia. These high $\bar{\kappa}$ features resemble the lobes of enhanced Rossby wave activity generated by convective heating at the equator. The increased upwelling associated with the breaking of these waves would be expected to generate variability in lower stratospheric water vapor (Ryu and Lee, 2010). The main source of convective variance in the 74–107 days time window used here to generate the $\bar{\kappa}$ map is the MJO. One would therefore expect the Rossby patterns here to reflect MJO activity. On the 100 hPa surface, MJO activity in the Indian Ocean is associated with a pair of anticyclones at opposite sides of the equator in the northern and southern Indian Ocean, similar to the patterns shown here in Fig. 8a (Weare, 2010).

Figure 7b shows the 40–107 days subseasonal time window selected for the CO $\bar{\kappa}$ map. The $N_2O$ $\bar{\kappa}$ map appeared to be noise and is not shown. The CO $\bar{\kappa}$ map shown in Fig. 8b does, however, appear to exhibit MJO related features. Figure 8c shows the $\bar{\kappa}$ map generated from 100 hPa temperature fluctuations and the RMM1 MJO index time series. The RMM1 $\bar{\kappa}$ map shows a boomerang or horseshoe shaped feature (Nishimoto and Shiotani, 2012) of high $\bar{\kappa}$ extending from the western equatorial Pacific, with what again appears to be symmetric Rossby lobes extending to the west. The CO subseasonal $\bar{\kappa}$ map (Fig. 8b) also shows a boomerang feature at the same location. In both patterns, the region of enhanced $\bar{\kappa}$ extends eastward along the equator to 150° E. The CO and RMM1 $\bar{\kappa}$ maps also show similar features over Africa and South America.





ACPD
12, 19571–19615, 2012

### 4.4 Multiyear time window

Figure 7 shows that, on multiyear timescales, the coherence between tropical mean temperatures at 100 hPa and tracer mixing ratios at 68 hPa varies very slowly with period. For the calculation of the $\bar{\kappa}$ maps on multiyear timescales, we therefore selected an identical 682–2048 days time window for all three tracers. The $H_2O$, CO, and $N_2O$ $\bar{\kappa}$ maps associated with this time window are shown in Fig. 9a, c, d. In general, the $\bar{\kappa}$ maps generated using the multiyear time window show no resemblance to the corresponding $\bar{\kappa}$ maps using the subseasonal time window. The dynamical mechanisms which regulate the transport of chemical tracers into the stratosphere on multiyear timescales are clearly different from the mechanisms which control this transport on subseasonal timescales.

The multiyear $H_2O$ $\bar{\kappa}$ map given in Fig. 9a shows that $\bar{\kappa}$ is enhanced at almost all longitudes within the 15° S–15° N latitude band except the eastern Pacific (90–180° W). Within this band, there are areas of larger $\bar{\kappa}$ over South America, the Indian Ocean, and the maritime continent. Large $\bar{\kappa}$ at a particular grid point does not neccessarilly imply that air parcels advected through this grid point are dehydrated by cold anomalies at that location. At the 100 hPa level, monthly mean temperatures are strongly correlated across distances of several thousand kms (Folkins, 2012). Rather than being sites of active dehydration, some of the large values of $\bar{\kappa}$ on the 100 hPa surface can probably be attributed to a coherence with the temperature fluctuations of a region where dehydration does occur. Regions of highest final dehydration density have been identified using trajectory models (e.g. Schoeberl and Dessler, 2011). The dehydration regions fall within the enhanced $\bar{\kappa}$ regions shown in Fig. 9a. There are also several regions of enhanced $\bar{\kappa}$ that are associated with very weak dehydration density, particularly the Indian Ocean. Regions where final dehydration occurs should exhibit enhanced $\bar{\kappa}$, but the reverse need not be true.

Figure 9c shows the multiyear CO $\bar{\kappa}$ map. The most prominent features of this map are the large regions of high $\bar{\kappa}$ in the subtropical Pacific on both sides of the equator.





ACPD
12, 19571–19615, 2012

Figure 10 shows the $\bar{\kappa}$ maps associated with temperature anomalies on the 100 hPa surface, and the U50 and the global ENSO indices. The Pacific dipole pattern (Randel et al., 2000; Zhou et al., 2004; Trenberth and Smith, 2006) is a common feature of both maps. On multiyear timescales, CO anomalies in the lower stratosphere are coherent with temperature variability on the 100 hPa surface that is associated with the QBO and ENSO.

The Pacific dipole is usually associated with ENSO (Randel et al., 2000; Zhou et al., 2004; Trenberth and Smith, 2006), whereas the QBO is associated with zonally symmetric temperature anomalies more strongly confined to the tropics (Huesmann and Hitchman, 2001; Pascoe et al., 2005; Liang et al., 2011). During the MLS observing period used here (2005–2010), the fact that the QBO and ENSO were mostly in phase (Liang et al., 2011) could account for the similarity of the QBO and ENSO $\bar{\kappa}$ maps shown in Fig. 10 .

Figure 9d shows the multiyear $N_2O$ $\bar{\kappa}$ map. This pattern does not show a Pacific dipole, but does show a boomerang shaped structure in the West Pacific. This pattern is associated with enhanced convective heating along the equator (Tian et al., 2006), and was previously seen in the RMM1 $\bar{\kappa}$ pattern.

## 5 Lagged correlation map for $H_2O$

The relationship between temperature anomalies on the 100 hPa surface and the mixing ratios of chemical tracers in the lower stratosphere can also be studied using lagged correlation maps. The temperature and tracer anomalies are first band pass filtered using a particular time window. The correlation between the temperature anomaly time series at a particular grid point and the mean tracer mixing ratio is then calculated with a particular time lag. Figure 9b shows the lagged correlation map for $H_2O$ using the multiyear time window and a 140 days time lag. This value of the time lag resulted in the largest average correlation over the 30° S–30° N latitude range. The lagged correlation map is very similar to the $\bar{\kappa}$ map, but does exhibit a stronger dipole structure in





ACPD
12, 19571–19615, 2012

the eastern Pacific than the multiyear $H_2O$ $\bar{\kappa}$ map. Figure 10 shows that this feature is associated with both QBO and ENSO variability, during the 2005–2010 time period considered here. Cold temperature anomalies within the Pacific dipole pattern are associated, on the 100 hPa surface, with positive ENSO phase (i.e. El Nino) (Weare, 2008).

For CO and $N_2O$, the time lag which maximized the correlation was not well defined. Lagged correlation maps for these tracers are therefore not shown.

## 6 Weighted mean time lags

At a given frequency $\omega$, the time lag between the chemical tracer (here $H_2O$) and 100 hPa temperature anomalies is equal to the phase spectrum ($\Phi_{T,H_2O}(\omega)$) divided by frequency ($\omega$).

$$\tau(\omega) = \frac{\Phi_{T,H_2O}(\omega)}{\omega} \tag{8}$$

Over a particular frequency window, $[\omega_1, \omega_2]$, we define the following effective coherence weighted mean time lag.

$$\bar{\tau} = \frac{\int_{\omega_1}^{\omega_2} \kappa^2_{T,H_2O}(\omega)\left(\frac{\Phi_{H_2O}(\omega)}{\omega}\right)d\omega}{\int_{\omega_1}^{\omega_2} \kappa^2_{T,H_2O}(\omega)d\omega} \tag{9}$$

We used the above expression to calculate the mean time lags in the subseasonal and multiyear time windows. Figure 11a–c shows subseasonal $\bar{\tau}$ vs. $\bar{\kappa}$ scatterplots for the three tracers. The thick solid lines indicate the mean dependence of $\bar{\tau}$ on $\bar{\kappa}$. One would expect $\bar{\tau}$ to converge to a physically significant value for larger values of $\bar{\kappa}$. This is not the case for $N_2O$, where the mean value of $\bar{\tau}$ is near zero for all $\bar{\kappa}$. However, this is consistent with our previous finding of the lack of any physically significant relationship between the $N_2O$ and 100 hPa temperature anomalies on subseasonal timescales. For CO, $\bar{\tau}$ converges to 5 days at large $\bar{\kappa}$. For $H_2O$, the mean time lag appears to decrease at large $\bar{\kappa}$. However, this decrease may be attributable to the lower number of grid cells with high $\bar{\kappa}$. For $\bar{\kappa}$ larger than 0.4, the mean time lags for $H_2O$ and CO in the subseasonal time windows are 2.51 and 3.16 days, respectively.

The subseasonal time lags of 2.51 and 3.16 days for $H_2O$ and CO are much smaller than would be expected to occur in association with changes in stratospheric entry mixing ratio. Using an annual mean ascent rate of $0.25\,\mathrm{mm\,s^{-1}}$ (Randel et al., 2008), the timescale for a change in stratospheric entry mixing ratio of a tracer to be advected by slow ascent to the center of the 68 hPa MLS kernel is roughly 100 days. On subseasonal timescales, the fluctuations in lower stratospheric $H_2O$ and CO that are coherent with 100 hPa temperature can therefore be attributed to the effect of upwelling fluctuations on the local tendency for vertical advection.

Figure 11d shows that, on multiyear timescales, the mean value of the $H_2O$ $\bar{\tau}$ converges to 200 days at high $\bar{\kappa}$. For $\bar{\kappa}$ larger than 0.4, the mean multiyear $H_2O$ time lag is 140 days. This time lag is roughly equal to the time required for an air parcel to be advected by slow ascent the 2.2 km vertical distance from 100 hPa ($\sim$16.6 km) to the center of the 68 hPa ($\sim$18.8 km) averaging kernel ($\sim$100 days). On multiyear timescales, the fluctuations in lower stratospheric water vapor that are coherent with 100 hPa temperature originate mainly from changes in the stratospheric entry mixing ratio.

For $H_2O$ (and other ice soluble tracers), there is a direct physical mechanism which couples TTL temperature fluctuations to changes in the mean stratospheric entry mixing ratio (Fueglistaler and Haynes, 2005). Dry tracers such as CO and $N_2O$ are not coupled to 100 hPa temperature fluctuations through the Clausius-Clapeyron relationship. However, there can be an indirect coupling mediated through changes in convective outflow. Cold anomalies in the TTL are ordinarilly coupled to increases in upwelling (Randel et al., 2002). The primary mass source for this upwelling is outflow from deep convection. If the upwelling mass flux increases, a higher fraction of deep convective



ACPD
12, 19571–19615, 2012

outflow must ascend into the stratosphere. This can be accomplished either by an increase in the altitude of convective outflow, or by a decrease in the Level of Zero radiative Heating (LZH). Both of these changes appear to occur in response to increased upwelling during Northern Hemisphere winter (Folkins et al., 2006). The relative effect of this mechanism on tracer mixing ratios should be largest at heights where the convectively induced changes in the tracer age spectrum (the elapsed time since convective detrainment) are comparable with the age of the tracer itself. This is most likely to occur in the TTL where high altitude outflow occurs, and less likely to occur in the lower stratosphere where air parcels are much older.

The solid line in Fig. 11e shows the dependence of the mean multiyear CO $\bar{\tau}$ on $\bar{\kappa}$. There is a tendency toward positive $\bar{\tau}$ at larger $\bar{\kappa}$. The mean $\bar{\tau}$ for $\bar{\kappa}$ larger than 0.4 is 33 days. This time lag is significantly shorter than the timescale associated with upward transport from 100 to 68 hPa ($\sim$ 100 days). It is therefore unlikely that the multiyear anomalies in lower stratospheric CO originate mainly from changes in stratospheric entry mixing ratio (e.g. from changes in convective outflow). However, the roughly tenfold increase in the time lag in going from subseasonal to multiyear timescales (3.16 days to 33 days) is roughly consistent with the increase in the subseasonal to multiyear time windows (from 40–107 days to 682–2048 days). The average phase offset between 100 hPa temperature and 68 hPa CO fluctuations in the subseasonal time window is therefore roughly equal to the average phase offset in the multiyear time window. This suggests that the multiyear 68 hPa CO fluctuations are also coupled to 100 hPa temperature fluctuations mainly through the effect of upwelling on the local tendency for vertical advection.

Figure 11f shows that the mean multiyear $\bar{\tau}$ for $N_2O$ converges to roughly −50 days for large $\bar{\kappa}$. On multiyear timescales, $N_2O$ anomalies in the lower stratosphere therefore precede 100 hPa temperature anomalies. The dynamical mechanism most likely to give rise to this kind of downward phase propagation is the QBO, which descends at rate of approximately 1 km per month (Baldwin et al., 2001). This rate of descent would be consistent with a 65 day time lag for the 2.2 km descent from the center of the





ACPD
12, 19571–19615, 2012

68 hPa ($\sim$ 18.8 km) $N_2O$ averaging kernel to the 100 hPa ($\sim$ 16.6 km) level. The similarity of these timescales, and the prominence of the QBO related features in the $\bar{\kappa}$ map (for the 2005–2010 period), indicates that the multiyear variability of $N_2O$ in the lower stratosphere is directly induced by the QBO. This is in contrast, for example, to the case of $H_2O$, where the QBO induced variability occurs indirectly through modulations in TTL temperature, which then subsequently affect the $H_2O$ stratospheric entry mixing ratio (Fueglistaler and Haynes, 2005).

The time lag plots shown in Fig. 12 demonstrate that, while the lower stratospheric water vapor fluctuations on subseasonal timescales are mainly generated by the effect of upwelling on the local tendency for vertical advection, water vapor fluctuations on multiyear timescales are mainly generated by fluctuations in the stratospheric entry mixing ratio. Figure 12a and c shows scatterplots of $\bar{\kappa}$ against annual mean temperature for each grid point on the 100 hPa surface. In the subseasonal time window, $\bar{\kappa}$ is almost independent of temperature. In the multiyear time window, there is a sharp increase in $\bar{\kappa}$ for temperatures colder than 194 K. These results are also consistent with the view that, although dehydration plays a minor role in lower stratospheric water vapor fluctuations on subseasonal timescales, TTL dehydration dominates lower stratospheric water variability on multiyear timescales.

In Fig. 12b the subseasonal $\bar{\tau}$ for $H_2O$ is plotted against annual mean temperature. The mean $\bar{\tau}$ is near zero for most values of temperature, but sharply increases to 10 days for temperatures less than 194 K. The origin of the increase in $\bar{\tau}$, despite the absence of an increase in $\bar{\kappa}$ is unclear. One possibility is that dehydration is playing a minor role in water vapor variability on subseasonal timescales. Because of the 100 days timescale for vertical advection from 100 hPa to the 68 pressure surface ($\sim$ 100 days), a small amount of TTL dehydration could generate a $\bar{\tau} \sim 10$ days at cold temperatures, while introducing only a small increase in $\bar{\kappa}$.

Figure 12d shows a scatterplot of the multiyear $\bar{\tau}$ for $H_2O$ plotted against annual mean temperature. There is a gradual increase in $\bar{\tau}$ at colder temperatures, reaching a





ACPD
12, 19571–19615, 2012

value close to 180 days for annual mean temperaures equal to 192 K. This increase is also consistent with an increasing role for dehydration at colder temperature.

## 7 Discussion and conclusion

We have examined the coherence in the tropics between temperature fluctuations on the 100 hPa surface and fluctuations in the lower stratospheric mixing ratios of $H_2O$, CO, and $N_2O$. Due to changes in the relative importance of different dynamical modes at different timescales, we have done separate calculations of the coherence in the subseasonal and multiyear time windows. On subseasonal timescales, the dominant features in the coherence pattern between fluctuations in 100 hPa temperature and water vapor are two Rossby lobes in the Indian Ocean extending symmetrically from both sides of the equator. The 68 hPa $H_2O$ mixing ratio anomalies are almost synchronous with the anomalies in 100 hPa temperature. At larger values of coherence (the $\bar{\kappa}$ statistic), the 68 hPa water vapor anomalies lag fluctuations in 100 hPa temperature by 2.5 days. On subseasonal timescales, the variability of water vapor in the lower tropical stratosphere is therefore dominated by variability in upwelling associated with the dissipation of Rossby waves (i.e. the BLN mechanism). However, the increase in the time lag $\bar{\tau}$ at colder temperatures is consistent with a minor role for dehydration in the subseasonal time window.

The spatial pattern of the coherence between lower stratospheric water vapor and 100 hPa temperature anomalies on multiyear timescales has no resemblance to the coherence pattern on subseasonal time scales. Whereas the subseasonal coherence pattern is dominated by two Rossby lobes, and is associated with values of $\bar{\kappa}$ that are independent of temperature, the multiyear coherence pattern covers a much larger geographic area and is strongly shaped by the annual mean pattern in 100 hPa temperature. In particular, the mean value of the multiyear $\bar{\kappa}$ increases sharply for annual mean temperatures colder than 194 K. In addition, the time lag between the multiyear anomalies in lower stratospheric water vapor and 100 hPa temperature increases with





ACPD
12, 19571–19615, 2012

both colder temperature and higher $\bar{\kappa}$, approaching a maximum value of 200 days. This timescale is equal to the time required for the vertical ascent of an air parcel from the 100 hPa surface to the top of the 68 hPa MLS $H_2O$ kernel. These results demonstrate that the multiyear variability in lower stratospheric water vapor is dominated by temperature fluctuations in the TTL which affect the water vapor stratospheric entry mixing ratio by modulating the amount of dehydration. It should be noted, however, that due to long distance correlations between temperature fluctuations on the 100 hPa surface, not all locations on the 100 hPa surface with large $\bar{\kappa}$ are likely to play a role in the dehydration of air parcels entering the stratosphere.

The rate of lower stratospheric upwelling from the BLN mechanism can be expected to be modulated by changes in both the intensity and location of tropical convection (Ryu and Lee, 2010). As the main source of variability of tropical convection in the subseasonal window, the MJO would therefore be expected to modulate the rate of lower stratospheric upwelling in this frequency range. We compared the spatial pattern of the coherence between the subseasonal anomalies in lower stratospheric CO and 100 hPa temperature to the spatial pattern of the coherence between the RMM1 MJO index and 100 hPa temperature. Both coherence patterns were evaluated over the 1 January 2005–31 December 2010 time interval. The two patterns were very similar, especially in the western tropical Pacific. In this region, both patterns exhibited a typical Gill type response with Rossby lobes spreading to the west and a Kelvin response spreading east toward the dateline. The MJO therefore plays a significant role in modulating the variability of lower stratospheric CO on subseasonal timescales. This finding is consistent with previous results showing that the MJO affects the distribution of ozone (Weare, 2010) and water vapor (Mote et al., 1998) in the lower tropical stratosphere, and the variability of CO in the TTL (Wong and Dessler, 2007).

The map of the coherence between the multiyear lower stratospheric CO and 100 hPa anomalies exhibited a strong Pacific dipole. This feature is usually characteristic of ENSO (Randel et al., 2000; Zhou et al., 2004; Trenberth and Smith, 2006). However, during the time period analyzed here, this pattern was coherent with both the

QBO and ENSO, so that the relative roles of these multiyear dynamical modes could not be differentiated. However, for larger values of $\bar{\kappa}$, the phase difference between the CO and 100 hPa temperature anomalies in the multiyear time window was similar to the phase difference in subseasonal time window. This suggests that the main mechanism through which variability in lower stratospheric upwelling generated CO anomalies on multiyear timescales was also through modulations of the local tendency for vertical advection.

In global chemistry climate models, it is often difficult to know whether the mechanisms for Stratosphere-Troposphere Exchange (STE) and TTL dehydration are being accurately modelled. This is partly because many of the STE exchange mechanisms involve small scale convective or cloud scale processes that are parameterized rather than explicitly modelled, and also because of difficulties in making more general conclusions from a limited number of in situ measurements. However, the statistical methods used here could be applied to output from climate models. Accurate simulations of the coherence between 100 hPa temperature fluctuations and the anomalies in lower stratospheric tracers, in different time windows, would give greater credibility to the future trends in stratospheric chemical constituents predicted by these models (Butchart et al., 2011). This type of analysis would be particularly important in the case of water vapor. The transport of condensable tracers like water vapor through the TTL is affected by a larger number of physical mechanisms than the transport of dry tracers, and calculations have suggested that past and future trends in stratospheric water vapor can exhibit a significant radiative forcing on climate (Solomon et al., 2010).

## Appendix A

### Comparison of MLS and ACE water vapor

Figure 13 shows a scatter plot of tropical mean daily ACE v3.0 and MLS v3.3 $H_2O$ values at 68 hPa. We first extracted all available ACE data from the height range

16.5–19.5 km during the period 2005–2010, and removed values whose statistical errors were more than 10 % of the actual value. Most of the ACE measurements in the tropics occur during February, April, August, and October. This short time coverage plus the data quality filtering we deployed reduced the number of data points with which we made a comparison with MLS to 193. The four ACE grid heights were converted to pressure levels using a tropical mean pressure profile. A simple linear interpolation was then done to compute ACE $H_2O$ at 68 hPa. The thick solid line in Fig. 13 represents the pairs of class means of the two data sets when each grouped into 14 bins with a bin size of 0.150 ppmv. Due to differences in weighting functions, viewing geometry, and sampling, there is no unique way to compare the two measurements. However, the ACE and MLS $H_2O$ measurements are in good overall agreement ($r$ = 0.778).

*Acknowledgements.* MLS and MERRA data have been acquired from NASA GES-DISC server. NCEP Reanalysis data provided by the NOAA/OAR/ESRL PSD, Boulder, Colorado, USA, from their web site at http://www.esrl.noaa.gov/psd/. ECMWF ERA-Interim data used in this study have been obtained from the ECMWF Data Server. This research was funded by the Canadian Space Agency (CSA) and the Natural Science and Engineering Research Council of Canada (NSERC). The authors would like to thank Eric Oliver for his constructive suggestions.

## References

Baldwin, M. P., Gray, L. J., Dunkerton, T. J., Hamilton, K., Haynes, P. H., Randel, W. J., Holton, J. R., Alexander, M. J., Hirota, I., Horinouchi, T., Jones, D. B. A., Kinnersley, J. S., Marquardt, C., Sato, K., and Takahashi, M.: The quasi-biennial oscillation, Rev. Geophys., 39, 179–229, doi:10.1029/1999RG000073, 2001. 19591

Bernath, P. F., McElroy, C. T., Abrams, M. C., Boone, C. D., Butler, M., Camy-Peyret, C., Carleer, M., Clerbaux, C., Coheur, P.-F., Colin, R., DeCola, P., DeMazière, M., Drummond, J. R., Dufour, D., Evans, W. F. J., Fast, H., Fussen, D., Gilbert, K., Jennings, D. E., Llewellyn, E. J., Lowe, R. P., Mahieu, E., McConnell, J. C., McHugh, M., McLeod, S. D., Michaud, R., Midwinter, C., Nassar, R., Nichitiu, F., Nowlan, C., Rinsland, C. P., Rochon, Y. J., Rowlands, N., Semeniuk, K., Simon, P., Skelton, R., Sloan, J. J., Soucy, M.-A., Strong, K., Tremblay, P., Turnbull, D., Walker, K. A., Walkty, I., Wardle, D. A., Wehrle, V., Zander, R., and Zou, J.: Atmospheric Chemistry Experiment (ACE): Mission overview, Geophys. Res. Lett., 32, L15S01, doi:10.1029/2005GL022386, 2005. 19574, 19577

Boehm, M. T. and Lee, S.: The implications of tropical Rossby waves for tropical tropopause cirrus formation and for the equatorial upwelling of the Brewer-Dobson Circulation, J. Atmos. Sci., 60, 247–261, doi:10.1175/1520-0469(2003)060<0247:TIOTRW>2.0.CO;2, 2003. 19573

Bosilovich, M. G., Chen, J., Robertson, F. R., and Adler, R. F.: Evaluation of global precipitation in reanalyses, J. Appl. Meteorol. Clim., 47, 2279–2299, doi:10.1175/2008JAMC1921.1, 2008. 19578

Bouttier, F. and Rabier, F.: The operational implementation of 4D-Var, ECMWF Newsletter, 2–5, 1997. 19578

Butchart, N., Charlton-Perez, A. J., Cionni, I., Hardiman, S. C., Haynes, P. H., Krüger, K., Kushner, P. J., Newman, P. A., Osprey, S. M., Perlwitz, J., Sigmond, M., Wang, L., Akiyoshi, H., Austin, J., Bekki, S., Baumgaertner, A., Braesicke, P., Brühl, C., Chipperfield, M., Dameris, M., Dhomse, S., Eyring, V., Garcia, R., Garny, H., Jöckel, P., Lamarque, J.-F., Marchand, M., Michou, M., Morgenstern, O., Nakamura, T., Pawson, S., Plummer, D., Pyle, J., Rozanov, E., Scinocca, J., Shepherd, T. G., Shibata, K., Smale, D., Teyssèdre, H., Tian, W., Waugh, D., and Yamashita, Y.: Multimodel climate and variability of the stratosphere, J. Geophys. Res., 116, D05102, doi:10.1029/2010JD014995, 2011. 19595

Calvo, N., Garcia, R. R., and Marsh, W. J. R. D. R.: Dynamical mechanism for the increase in tropical upwelling in the lowermost tropical stratosphere during warm ENSO events, J. Atmos. Sci., 67, 2331–2340, doi:10.1175/2010JAS3433.1, 2010. 19573

D'Amelio, M. T. S., Gatti, L. V., Miller, J. B., and Tans, P.: Regional $N_2O$ fluxes in Amazonia derived from aircraft vertical profiles, Atmos. Chem. Phys., 9, 8785–8797, doi:10.5194/acp-9-8785-2009, 2009. 19581

Dee, D. P. and Uppala, S.: Variational bias correction of satellite radiance data in the ERA-Interim reanalysis, Q. J. Roy. Meteorol. Soc., 135, 1830–1841, doi:10.1002/qj.493, 2009. 19578

Duchon, C. E.: Lanczos filtering in one and two dimensions, J. Appl. Meteor., 18, 1016–1022, doi:10.1175/1520-0450(1979)018<1016:LFIOAT>2.0.CO;2, 1979. 19580

Folkins, I.: Height increase of the melting level stability anomaly in the tropics, Atmos. Chem. Phys. Discuss., 12, 11567–11594, doi:10.5194/acpd-12-11567-2012, 2012. 19587

Folkins, I., Bernath, P., Boone, C., Lesins, G., Livesey, N., Thompson, A. M., Walker, K., and Witte, J. C.: Seasonal cycles of $O_3$, CO, and convective outflow at the tropical tropopause, Geophys. Res. Lett., 33, L16802, doi:10.1029/2006GL026602, 2006. 19591

Fueglistaler, S. and Haynes, P. H.: Control of interannual and longer-term variability of stratospheric water vapor, J. Geophys. Res., 110, D24108, doi:10.1029/2005JD006019, 2005. 19573, 19590, 19592

Garcia, R. R. and Randel, W. J.: Acceleration of the Brewer Dobson Circulation due to increases in greenhouse gases, J. Atmos. Sci., 65, 2731–2739, doi:10.1175/2008JAS2712.1, 2008. 19573

Garny, H., Dameris, M., Randel, W., Bodeker, G. E., and Deckert, R.: Dynamically forced increase of tropical upwelling in the lower stratosphere, J. Atmos. Sci., 68, 1214–1233, doi:10.1175/2011JAS3701.1, 2011b. 19573

Gill, A.: Some simple solutions for heat-induced tropical circulations, Q. J. Roy. Meteor. Soc., 106, 447–462, 1980. 19575

Hans, V. S. and Francis, W. Z.: Statistical analysis in climate research, Cambridge University Press (Virtual Publishing), virtual Edn., 2003. 19582

Hendon, H. H. and Salby, M. L.: The life cycle of the Madden-Julian oscillation, J. Atmos. Sci., 51, 2225–2237, doi:10.1175/1520-0469(1994)051<2225:TLCOTM>2.0.CO;2, 1994. 19575

Holton, J. R., Haynes., P. H., McIntyre., M. E., Douglass., A. R., Rood., R. B., and Pfister, L.: Stratosphere-Troposphere Exchange, Rev. Geophys., 33, 403–439, doi:10.1029/95RG02097, 1995. 19573

Huesmann, A. S. and Hitchman, M. H.: The stratospheric quasibiennial oscillation in the NCEP reanalyses: Climatological structures, J. Geophys. Res., 106, 11859–11874., 2001. 19588

Jin, F.-F. and Hoskins, B. J.: The direct response to tropical heating in a baroclinic atmosphere., J. Atmos. Sci.,, 52, 307–319, 1995. 19575

Kalnay, E., Kanamitsu, M., Kistler, R., Collins, W., Deaven, D., Gandin, L., Iredell, M., Saha, S., White, G., Woollen, J., Zhu, Y., Chelliah, M., Ebisuzaki, W., Higgins, W., Janowiak, J., Mo, K. C., Ropelewski, C., Wang, J., Leetmaa, A., Reynolds, R., Jenne, R., and Joseph, D.: The NCEP/NCAR 40-year reanalysis project, B. Am. Meteorol. Soc., 77, 437–471, doi:10.1175/1520-0477(1996)077<0437:TNYRP>2.0.CO;2, 1996. 19578

Kerr-Munslow, A. M. and Norton, W. A.: Tropical wave driving of the annual cycle in tropical tropopause temperatures. Part I: ECMWF analyses, J. Atmos. Sci., 63, 1410–1419, doi:10.1175/JAS3697.1, 2006. 19573

Lambert, A., Read, W., Livesey, N. J., Santee, M., Manney, G., Froidevaux, L., Wu, D., Schwartz, M., Pumphrey, H., Jimenez, C., Nedoluha, G., Cofield, R. E., Cuddy, D. T., Daffer, W., Drouin, B., Fuller, R., Jarnot, R., Knosp, B. W., Pickett, H., Perun, V., Jucks, K., Toon, G., Stachnik, R., Urban, J., Murtagh, D., Elkins, J., and Atlas, E.: Validation of the Aura Microwave Limb Sounder middle atmosphere water vapor and nitrous oxide measurements, J. Geophys. Res., 112, D24S36, doi:10.1029/2007JD008724, 2007. 19577

Liang, C. K., Eldering, A., Gettelman, A., Tian, B., Wong, S., Fetzer, E. J., and Liou, K. N.: Record of tropical interannual variability of temperature and water vapor from a combined AIRS-MLS data set, J. Geophys. Res., 116, D06103, doi:10.1029/2010JD014841, 2011. 19588

Monier, E., Weare, B. C., and Gustafson, W. I.: The Madden-Julian oscillation wind-convection coupling and the role of moisture processes in the MM5 model, Clim. Dynam., 35, 435–447, doi:10.1007/s00382-009-0626-4, 2010. 19573

Mote, P. W., Dunkerton, T. J., and Pumphrey, H. C.: Subseasonal variations in lower stratospheric water vapor, Geophys. Res. Lett., 25, 2445–2448, doi:10.1029/98GL51847, 1998. 19594

Nishimoto, E. and Shiotani, M.: Seasonal and interannual variability in the temperature structure around the tropical tropopause and its relationship with convective activities, J. Geophys. Res, 117, D02104, doi:10.1029/2011JD016936, 2012. 19586

Norton, W. A.: Tropical wave driving of the annual cycle in tropical tropopause temperatures. Part II: Model results, J. Atmos. Sci., 63, 1420–1431, doi:10.1175/JAS3698.1, 2006. 19573

Oliver, E. C. J. and Thompson, K. R.: Madden-Julian Oscillation and sea level: Local and remote forcing, J. Geophys. Res., 115, C01003, doi:10.1029/2009JC005337, 2010. 19574, 19585

Pascoe, C. L., Gray, L. J., Crooks, S. A., Juckes, M. N., and Baldwin, M. P.: The quasi-biennial oscillation: Analysis using ERA-40 data, J. Geophys. Res., 110, D08105, doi:10.1029/2004JD004941, 2005. 19588

Priestley, M. B.: Spectral analysis and time series, Probability and mathematical statistics, London, Academic Press, 1981. 19583, 19585

Randel, W., Wu, F., and Gaffen, D.: Interannual variability of the tropical tropopause derived from radiosonde data and NCEP reanalyses, J. Geophys. Res., 105, 15509–15523, doi:10.1029/2000JD900155, 2000. 19580, 19588, 19594





ACPD
12, 19571–19615, 2012

Randel, W., Wu, F., Oltmans, S., Rosenlof, K., and Nedoluha, G.: Interannual changes of stratospheric water vapor and correlations with tropical tropopause temperatures, J. Atmos. Sci., 61, 2133–2148, doi:10.1175/1520-0469(2004)061<2133:ICOSWV>2.0.CO;2, 2004. 19573

Randel, W. J., Garcia, R. R., and Wu, F.: Time-dependent upwelling in the tropical lower stratosphere estimated from the zonal-mean momentum budget, J. Atmos. Sci., 59, 2141–2152, doi:10.1175/1520-0469(2002)059<2141:TDUITT>2.0.CO;2, 2002. 19590

Randel, W. J., Garcia, R., and Wu, F.: Dynamical balances and tropical stratospheric upwelling, J. Atmos. Sci., 65, 3584–3595, doi:10.1175/2008JAS2756.1, 2008. 19573, 19576, 19580, 19590

Randel, W. J., Garcia, R. R., Calvo, N., and Marsh, D.: ENSO influence on zonal mean temperature and ozone in the tropical lower stratosphere, J. Geophys. Res., 36, L15822, doi:10.1029/2009GL039343, 2009. 19573

Read, W., Lambert, A., Bacmeister, J., Cofield, R., Christensen, L., Cuddy, D., Daffer, W., Drouin, B., Fetzer, E., Froidevaux, L., Fuller, R., Herman, R., Jarnot, R. F., Jiang, J. H., Jiang, Y., Kelly, K., Knosp, B., Pumphrey, H., Rosenlof, K., Sabounchi, X., Santee, M., Schwartz, M., Snyder, W., Stek, P., Su, H., Takacs, L., Thurstans, R., Vomel, H., Wagner, P., and Waters, J.: Upper tropospheric and lower stratospheric $H_2O$ and relative humidity with respect to ice validation, J. Geophys. Res., 112, D24S35, doi:10.1029/2007JD008752, 2007. 19577

Rienecker, M., Suarez, M., Todling, R., Bacmeister, J., Takacs, L., Liu, H.-C., Gu, W., Sienkiewicz, M., Koster, R., Gelaro, R., Stajner, I., and Nielsen, J.: The GEOS-5 Data Assimilation System-Documentation of versions 5.0.1 and 5.1.0, and 5.2.0. NASA Tech. Rep. Series on Global Modeling and Data Assimilation, NASA/TM, 27, 2008. 19578

Rienecker, M. M., Suarez, M. J., Gelaro, R., Todling, R., Bacmeister, J., Liu, E., Bosilovich, M. G., Schubert, S. D., Takacs, L., Kim, G.-K., Bloom, S., Chen, J., Collins, D., Conaty, A., da Silva, A., Gu, W., Joiner, J., Koster, R. D., Lucchesi, R., Reichle, R., and Woollen, J.: MERRA: NASA Modern-Era Retrospective Analysis for Research and Applications, J. Climate, 24, 3624–3648, doi:10.1175/JCLI-D-11-00015.1, 2011. 19578

Ryu, J.-H. and Lee, S.: Effect of tropical waves on the Tropical Tropopause Transition Layer upwelling, J. Atmos. Sci., 67, 3130–3148, doi:10.1175/2010JAS3434.1, 2010. 19573, 19575, 19586, 19594

Schoeberl, M. R. and Dessler, A. E.: Dehydration of the stratosphere, Atmos. Chem. Phys., 11, 8433–8446, doi:10.5194/acp-11-8433-2011, 2011. 19587





ACPD

12, 19571–19615, 2012

**Upwelling into the lower stratosphere**

Z. Engida and I. Folkins

Schoeberl, M. R., Douglass, A. R., Newman, P. A., Lait, L. R., Lary, D., Waters, J., Livesey, N., Froidevaux, L., Lambert, A., Read, W., Filipiak, M. J., and Pumphrey, H. C.: QBO and annual cycle variations in tropical lower stratosphere trace gases from HALOE and Aura MLS observations, J. Geophys. Res., 113, D05301, doi:10.1029/2007JD008678, 2008. 19573

Solomon, S., Rosenlof, K. H., Portmann, R. W., Daniel, J. S., Davis, S. M., Sanford, T. J., and Plattner, G.-K.: Contributions of stratospheric water vapor to decadal changes in the rate of global warming, Science, 327, 1219–1223, doi:10.1126/science.1182488, 2010. 19595

Tian, B., Waliser, D. E., Fetzer, E. J., Lambrigtsen, B. H., Yung, Y. L., and Wang, B.: Vertical moist thermodynamic structure and spatial-temporal evolution of the MJO in AIRS observations, J. Atmos. Sci., 63, 2462–2485, doi:10.1175/JAS3782.1, 2006. 19575, 19588

Ting, M. and Yu, L.: Steady response to tropical heating in wavy linear and nonlinear baroclinic models, J. Atmos. Sci., 55, 2565–2582, 1998. 19575

Trenberth, K. E. and Smith, L.: The vertical structure of temperature in the tropics: Different flavors of El Niño, J. Climate, 19, 4956–4973, 2006. 19588, 19594

Vömel, H., Barnes, J., Forno, R., Fujiwara, M., Hasebe, F., Iwasaki, S., Kivi, R., Komala, N., Kyro, E., Leblanc, T., Morel, B., Ogino, S., Read, W., Ryan, S., Saraspriya, S., Selkirk, H., Shiotani, M., Valverde-Canossa, J., and Whiteman, D.: Validation of Aura MLS water vapor by balloon borne cryogenic frostpoint hygrometer measurements, J. Geophys. Res, 112, D24S37, doi:10.1029/2007JD008698, 2007. 19577

Waters, J. W., Froidevaux, L., Harwood, R. S., Jarnot, R. F., Pickett, H. M., Read, W. G., Siegel, P. H., Cofield, R. E., Filipiak, M. J., Flower, D. A., Holden, J. R., Lau, G. K., Livesey, N. J., Manney, G. L., Pumphrey, H. C., Santee, M. L., Wu, D. L., Cuddy, D. T., Lay, R. R., Loo, M. S., Perun, V. S., Schwartz, M. J., Stek, P. C., Thurstans, R. P., Boyles, M. A., Chandra, K. M., Chavez, M. C., Gun-Shing, C., Chudasama, B. V., Dodge, R., Fuller, R. A., Girard, M. A., Jiang, J. H., Yibo, J., Knosp, B. W., LaBelle, R. C., Lam, J. C., Lee, K. A., Miller, D., Oswald, J. E., Patel, N. C., Pukala, D. M., Quintero, O., Scaff, D. M., Van Snyder, W., Tope, M. C., Wagner, P. A., and Walch, M. J.: The Earth Observing System Microwave Limb Sounder (EOS MLS) on the Aura Satellite, Geosci. Remote Sens., 44, 1075–1092, doi:10.1109/TGRS.2006.873771, 2006. 19574, 19576, 19577

Weare, B. C.: Multilag Singular Value Decomposition analysis of ENSO convection with tropical stratospheric temperature, J. Climate, 21, 6556–6568, doi:10.1175/2008JCLI2298.1, 2008. 19589





ACPD

12, 19571–19615, 2012

Upwelling into the lower stratosphere

Z. Engida and I. Folkins

Weare, B. C.: Madden-Julian Oscillation in the tropical stratosphere, J. Geophys. Res., 115, D17113, doi:10.1029/2009JD013748, 2010. 19586, 19594

Wheeler, M. C. and Hendon, H. H.: An all-season real-time multivariate MJO index: Development of an index for monitoring and prediction, Mon. Weather Rev., 132, 1917–1932, 2004. 19575, 19579

Wong, S. and Dessler, A. E.: Regulation of $H_2O$ and CO in tropical tropopause layer by the Madden-Julian oscillation, J. Geophys. Res., 112, D14305, doi:10.1029/2006JD007940, 2007. 19580, 19594

Zhang, C.: Madden-Julian Oscillation, Rev. Geophys., 43, RG2003, doi:10.1029/2004RG000158, 2005. 19573, 19584

Zhou, X. L., Geller, M. A., and Zhang, M.: Temperature fields in the tropical tropopause transition layer, J. Climate, 17, 2901–2908, doi:10.1175/1520-0442(2004)017<2901:TFITTT>2.0.CO;2, 2004. 19588, 19594





ACPD

12, 19571–19615, 2012

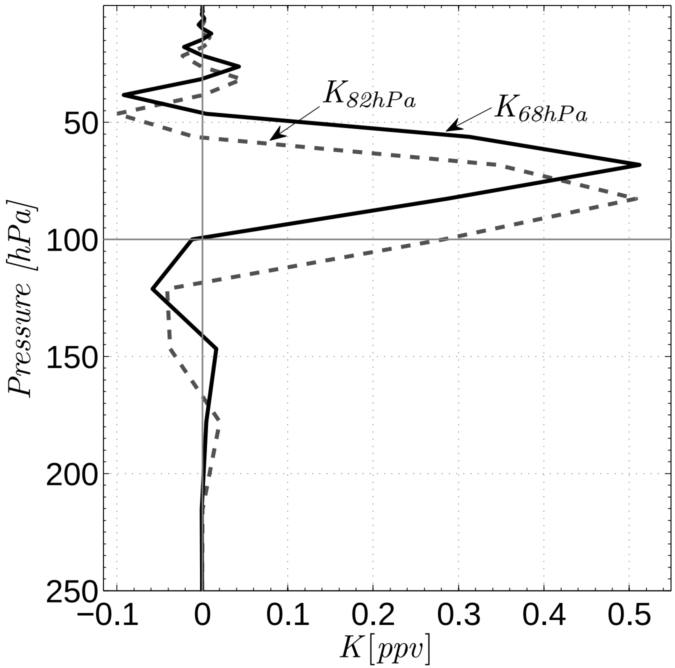


**Fig. 1.** Averaging kernels of MLS v3.3 $H_2O$. The solid line is for 68 hPa, while the dashed line is for 82 hPa pressure level.



Discussion Paper | Discussion Paper | Discussion Paper | Discussion Paper |

ACPD
12, 19571–19615, 2012

Upwelling into the lower stratosphere

Z. Engida and I. Folkins

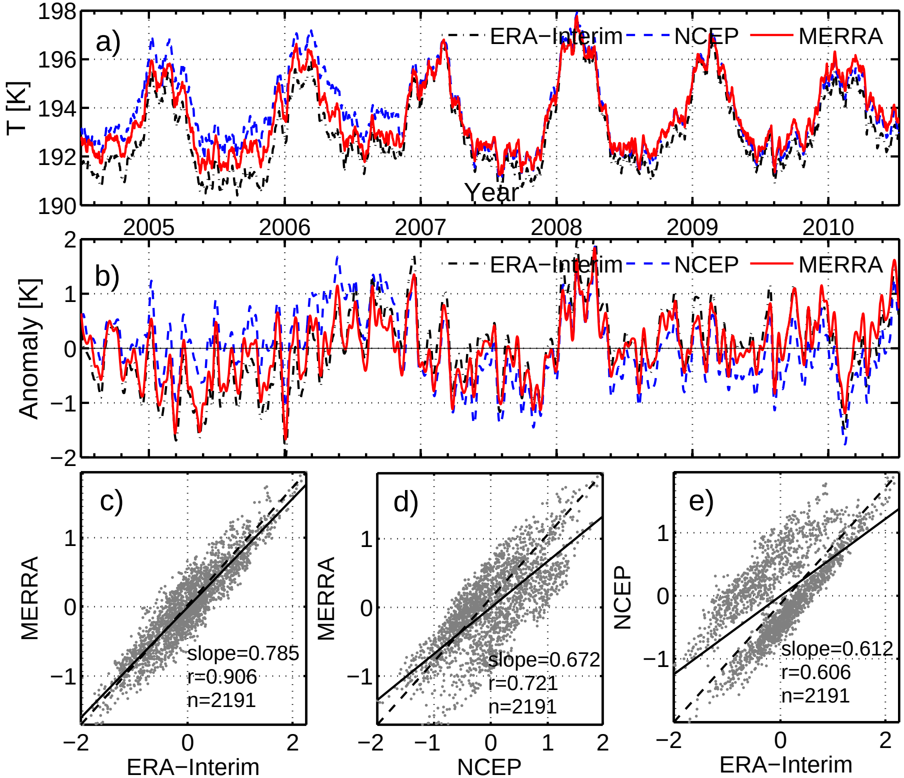


**Fig. 2.** Time series, of **(a)** 15° N–15° S average 100 hPa reanalyses temperatures and **(b)** deseasonalized, 15-day low pass filtered anomalies of those in **(a)**. Dark dotted line, blue dashed and red solid lines represent ERA-Interim, NCEP, and MERRA. Scatter plots showing comparison of the temperature anomalies of **(c)** MERRA vs ERA-Interim, **(d)** MERRA vs. NCEP and **(e)** NCEP vs ERA-Interim. Solid lines represent least square lines whose slopes are shown on lower left.





ACPD
12, 19571–19615, 2012

Upwelling into the lower stratosphere

Z. Engida and I. Folkins

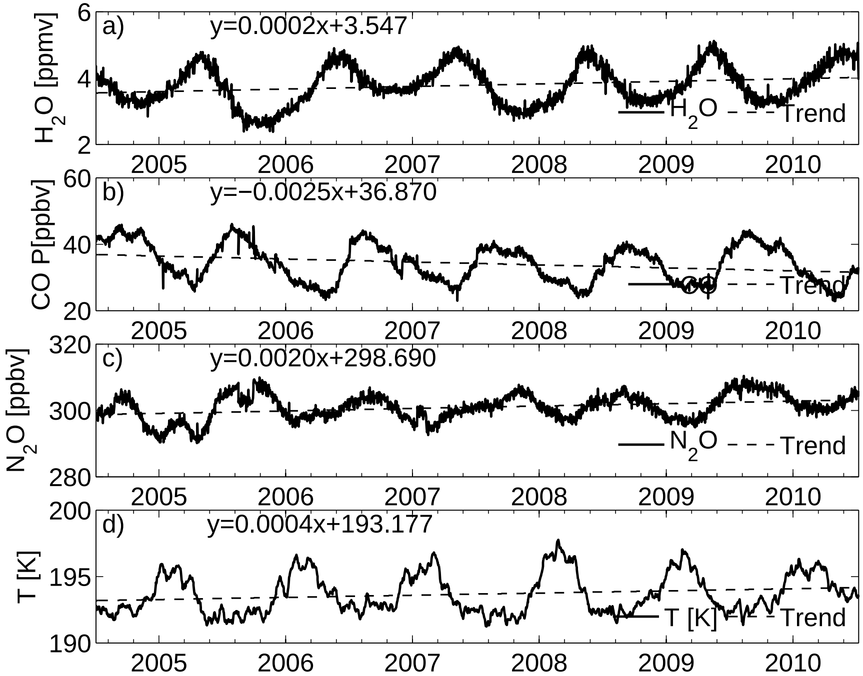


**Fig. 3.** Time Series of Tropical mean daily values of MLS **(a)** $H_2O$, **(b)** CO and **(c)** $N_2O$ and **(d)** 15° N–15° S average 100 hPa MERRA temperature. Dashed lines are trend lines whose equations are shown on top.

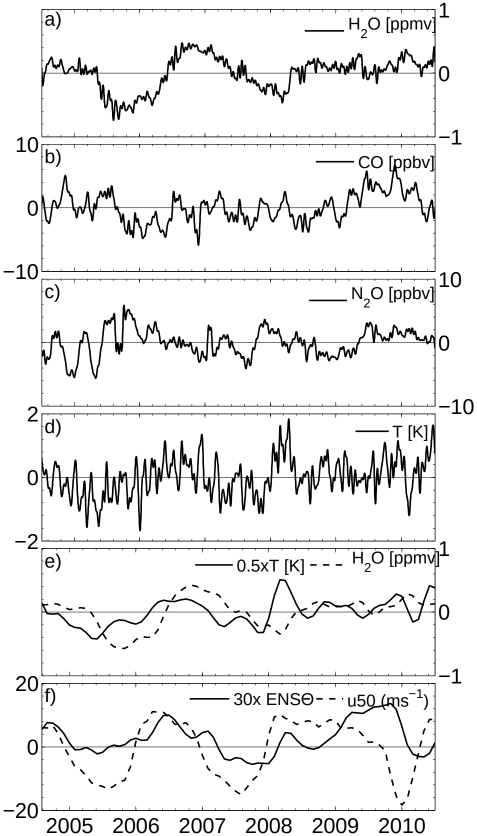


**Fig. 4.** The deseasonalized, detrended, and 15-day low pass filtered anomalies of the time series shown in Fig. 3. **(a)** $H_2O$, **(b)** CO, **(c)** $N_2O$, **(d)** Temperature, and **(e)** Re-scaled Temperature (solid) and $H_2O$ (dashed) monthly mean anomalies, **(f)** zonal mean 50 hPa wind anomaly (solid) and re-scaled global ENSO index (dashed).





ACPD

12, 19571–19615, 2012

Upwelling into the lower stratosphere

Z. Engida and I. Folkins

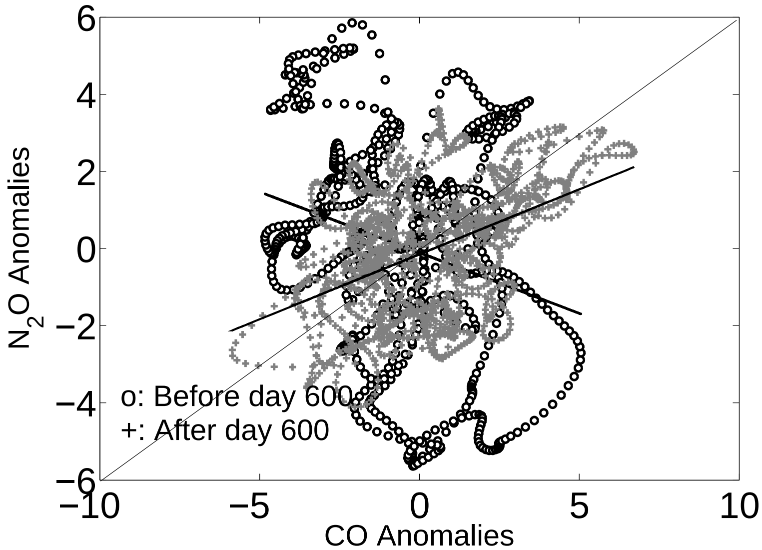


**Fig. 5.** Scatter plot of anomalies of CO and $N_2O$ from Fig. 4: data pairs before and after the first 600 days of 2191 days shown in dark "o" and grey "+" marks. (See the text for slopes of the corresponding least square lines.)





ACPD
12, 19571–19615, 2012

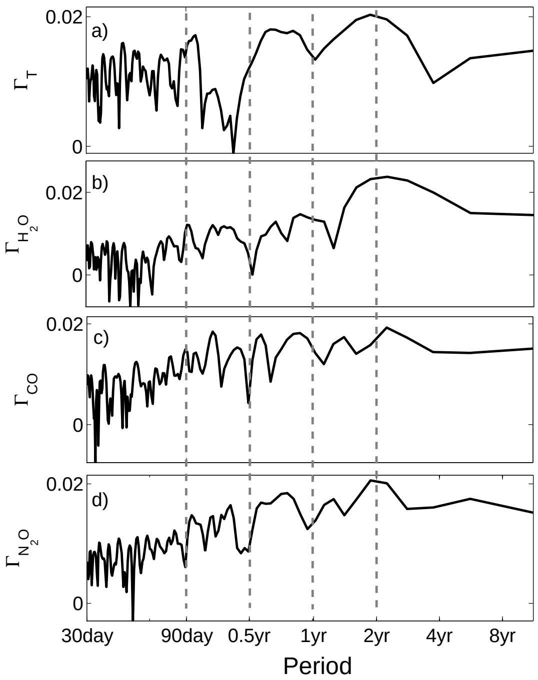


**Fig. 6.** Power Spectra for 15 day filtered **(a)** 100 hPa MERRA temperature anomalies (15° S–15° N mean) and 68 hPa MLS **(b)** $H_2O$, **(c)** CO, and **(d)** $N_2O$ anomalies (20° N–20° S mean).

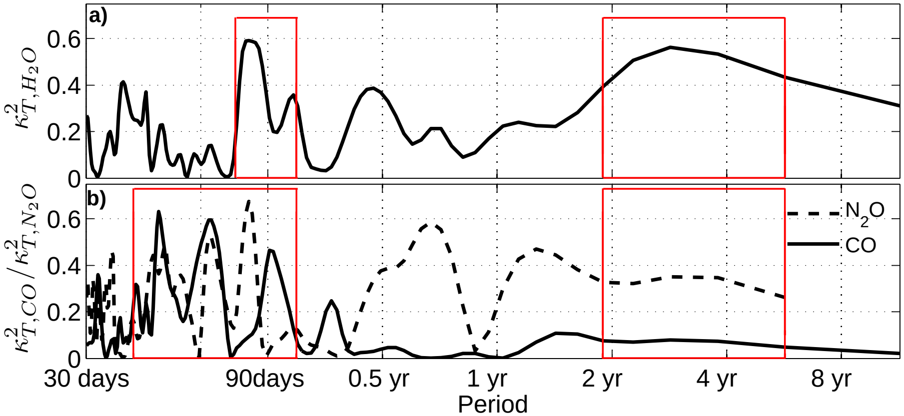


**Fig. 7.** $\kappa^2$ vs. period curves for 15 day filtered 100 hPa MERRA temperature anomalies (15° S–15° N mean) and **(a)** $H_2O$; **(b)** CO (solid line) and $N_2O$ (dashed line). The red boxes indicate the seasonal and multiyear time windows used for the various tracers.





ACPD
12, 19571–19615, 2012

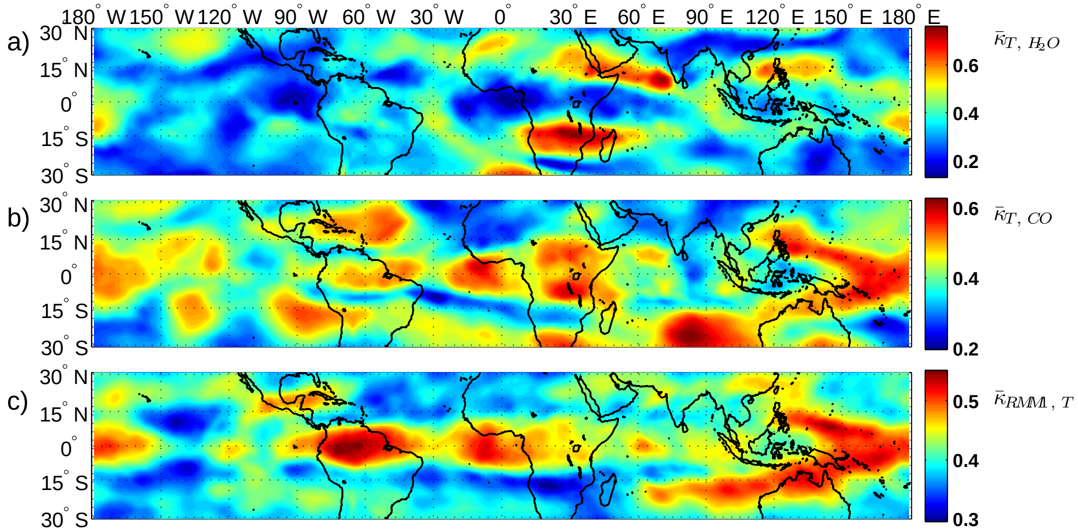


**Fig. 8.** $\bar{\kappa}$ maps for subseasonal window: **(a)** $\bar{\kappa}_{T,H_2O}$, **(b)** $\bar{\kappa}_{T,CO}$, **(c)** $\bar{\kappa}_{RMM1,T}$.





ACPD
12, 19571–19615, 2012

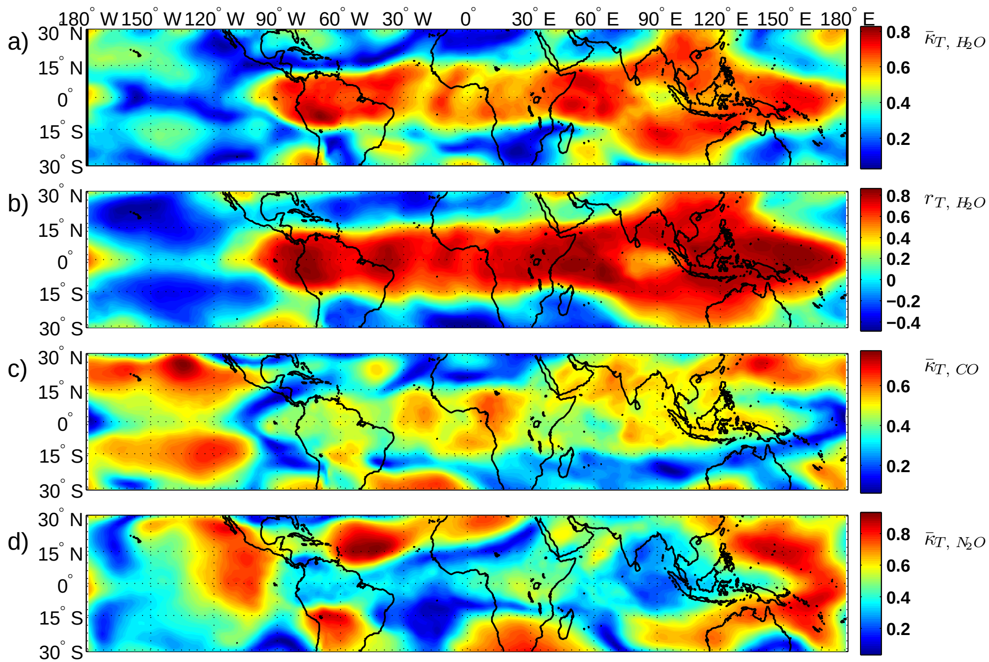


**Fig. 9. (a)** $\bar{\kappa}_{T,H_2O}$, **(b)** $r_{T,H_2O}$ using 140 day lag, **(c)** $\bar{\kappa}_{T,CO}$, **(d)** $\bar{\kappa}_{T,N_2O}$.





ACPD
12, 19571–19615, 2012

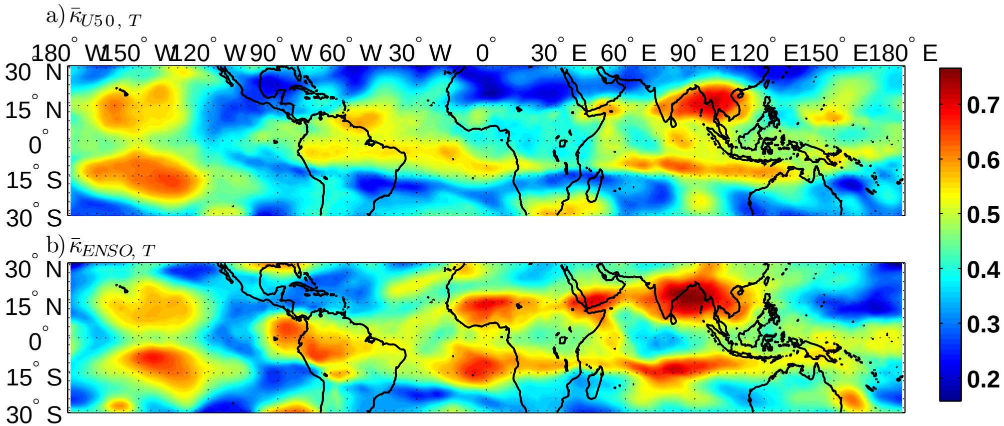


**Fig. 10.** $\bar{\kappa}$ using 100 hPa $T$ anomalies and **(a)** U50 and **(b)** global ENSO indices.





ACPD
12, 19571–19615, 2012

Upwelling into the lower stratosphere

Z. Engida and I. Folkins

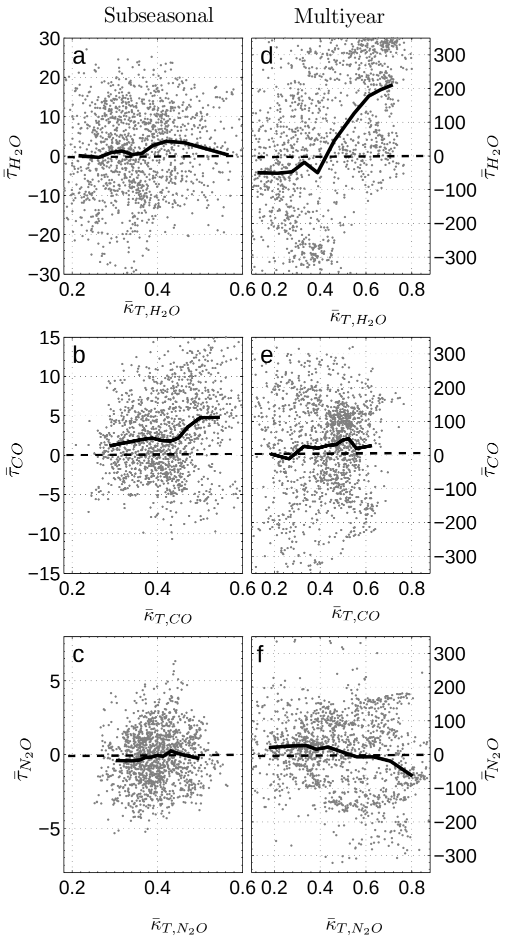


**Fig. 11.** Scatter plots of the mean time lag $\bar{\tau}$ against $\bar{\kappa}$ for the subseasonal **(a–c)** and multi-year **(d–f)** time windows. The solid lines refer to the mean dependence of $\bar{\tau}$ on $\bar{\kappa}$.





ACPD
12, 19571–19615, 2012

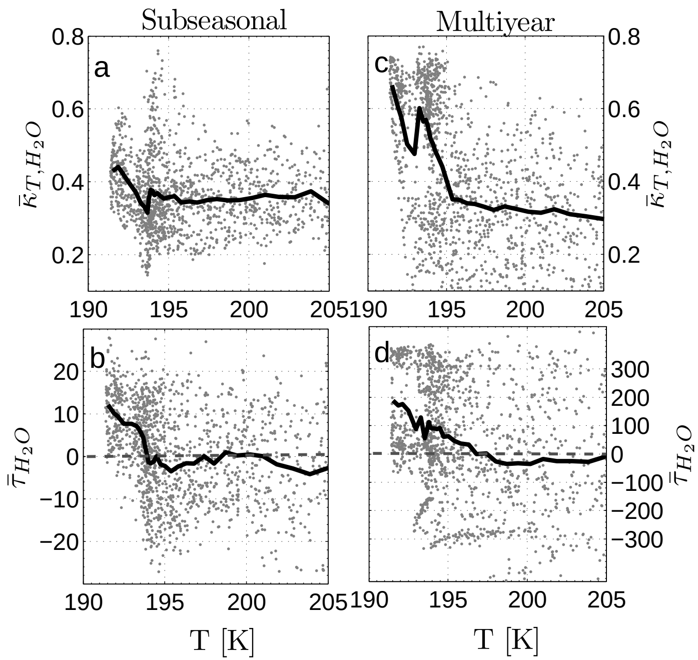


**Fig. 12.** **(a)** Subseasonal $\bar{\kappa}$ against annual mean MERRA temperature for grid boxes on the 100 hPa surface; **(b)** subseasonal $\bar{\tau}$ against annual mean 100 hPa MERRA temperature. Plots **(c)** and **(d)** are the same as **(a)** and **(b)**, except that $\bar{\kappa}$ and $\bar{\tau}$ refer to the multiyear time window. In each plot, the solid lines show the mean dependence of $\bar{\kappa}$, or $\bar{\tau}$, on temperature.





ACPD
12, 19571–19615, 2012

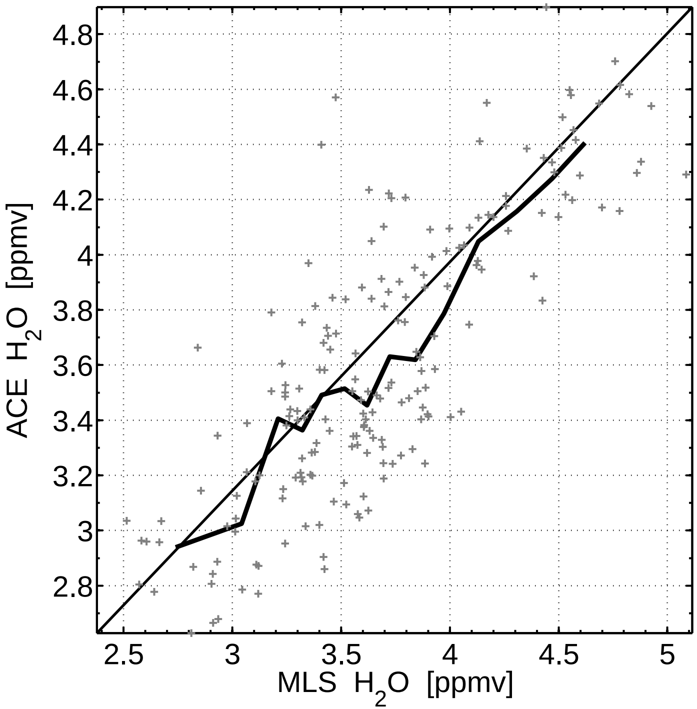


**Fig. 13.** A scatter plot of tropical mean (20° N–20° S) daily ACE and MLS $H_2O$ at 68 hPa. The dark solid line represents pairs of class means when the two data are binned into groups (ACE tangent heights are converted into equivalent pressure levels and simple interpolation used).





ACPD
12, 19571–19615, 2012

Upwelling into the lower stratosphere

Z. Engida and I. Folkins